



Quantitative evaluations of subtropical westerly jet simulations over East Asia based on multiple CMIP5 and CMIP6 GCMs

Bingqian Zhou^a, Shujuan Hu^{a,*}, Yongli He^a, Siyi Wang^a, Deqian Li^a, Guolin Feng^{b,c}

^a Key Laboratory for Semi-Arid Climate Change of the Ministry of Education, College of Atmospheric Sciences, Lanzhou University, Lanzhou 730000, China

^b Physical Science and Technology College, Yangzhou University, Yangzhou, China

^c Southern Marine Science and Engineering Guangdong Laboratory, Zhuhai, China



ARTICLE INFO

Keywords:

Model evaluation
East Asian subtropical westerly jet
CMIP5 GCMs
CMIP6 GCMs
Meridional temperature gradient

ABSTRACT

As a salient feature of the Asian monsoon system, the East Asian subtropical westerly jet (EASWJ) exerts significant impacts on weather and climate changes in China and even throughout East Asia. In this paper, we applied a new self-adaptive algorithm to detect the EASWJ, identify its boundaries, and then represent its characteristics by defining three indices: the intensity index, meridional displacement index, and width index. Compared to the reanalysis data, we carried out a comprehensive, objective, and quantitative EASWJ evaluation using historical experiments from multiple global climate models (GCMs) in the Coupled Model Intercomparison Project Phases 5 and 6 (CMIP5 and CMIP6). The results show that the multimodel ensemble mean (MME) of both CMIP5 and CMIP6 can simulate the characteristics of winter EASWJ well. While for the other three seasons, the MME of both phase models underestimate the 200-hPa zonal wind (U200) strength in the jet coverage area and overestimate the U200 outside the jet area, such simulation results weaken the meridional shear of the wind field. The EASWJ simulations from the CMIP5 GCMs had no consistent intensity or location characteristic tendencies, and most CMIP5 GCMs tended to simulate relatively wide-coverage jets. In contrast, most CMIP6 GCMs are inclined to simulate significantly weaker, wider, and more-northward jets. Compared to the predecessors in CMIP5, about half of CMIP6 GCMs significantly minimized the jet intensity bias, but remarkable errors were still observed in their jet location and coverage representations. Furthermore, the comparative analysis performed by classifying models based on their evaluated simulation results suggested that the simulated performance of the meridional temperature gradient was important for capturing the EASWJ characteristics. Further in-depth study of the causes of model differences is warranted to improve simulation results.

1. Introduction

The East Asian subtropical westerly jet (EASWJ) is a crucial component of the Asian monsoon system. Its seasonally north-jump and south-retreat are significantly correlated with the seasonal transition of the Asian atmospheric circulation (Ye et al., 1958; Li et al., 2020; He et al., 2020; Chiang et al., 2020). The EASWJ not only complexly interacts with the surrounding circulation systems, such as the western Pacific subtropical high and south Asia high (Liang and Wang, 1998; Lu, 2004; Lin and Lu, 2005; Schiemann et al., 2009; Du et al., 2016; Wei et al., 2017), but also has an important influence on climate and weather changes in East Asia (Lau et al., 2000; Lu et al., 2002; Yang et al., 2002; Liao et al., 2004; Kuang and Zhang, 2005; Xiao et al., 2016; Zhou et al., 2019). In particular, the position of the EASWJ is crucial in affecting the

precipitation pattern and intensity over China and even throughout East Asia (Tao et al., 1958; Lau et al., 2000; Li et al., 2004; Du et al., 2008; Qiang and Yang, 2008; Sampe and Xie, 2010; Dong et al., 2011; Shen et al., 2011; Liao and Zhang, 2013; Xie et al., 2015; Wang et al., 2017b; Li and Lu, 2017, 2018; Wang et al., 2019; Bao and You, 2019; Wang et al., 2021). In boreal summer, the southward movement of the EASWJ can cause abnormal precipitation increases in the Yangtze River Valley (YRV), which in turn significantly increases the risk of regional floods. The northward movement of the EASWJ can also cause abnormally increasing precipitation in North China (Kuang and Zhang, 2006; Du et al., 2009; Fang et al., 2009; Xuan et al., 2011; Wang et al., 2017b). Zhang et al. (2006) found that the displacement of the jet core between 140°E and 90°E in summer is related to the onset of the Mei-yu period and is thus critical for determining the beginning and end times of the

* Corresponding author.

E-mail address: hushuju@lzu.edu.cn (S. Hu).

Mei-yu period. Huang et al. (2015) found a positive correlation between the frequency of spring persistent rainfall and the “strong East Asian subtropical jet (EASJ)-weak East Asian polar front jet (EAPJ)” circulation pattern. Wang and Zuo (2016) found that in early summer, the intensified subtropical westerly jet in the East Asian continent caused precipitation to increase in the YRV. However, in midsummer, the enhanced subtropical westerly jet reduced precipitation in this region. Thus, the evolution of both the location and strength of the EASWJ have implications for precipitation in East Asia.

Based on the major climatic impacts of the EASWJ in East Asia, many previous studies have been conducted to evaluate the jet stream simulations and project the EASWJ changes output by the global climate models (GCMs) of the 5th Coupled Model Intercomparison Project (CMIP5; Taylor et al., 2012; Huang et al., 2013; Liang and Frauenfeld, 2014; Feng et al., 2014; Wang et al., 2017a; Huang et al., 2018; Brace-girdle et al., 2018). Xiao and Zhang (2013) found that FGOALS-g2 model had a better performance when simulating the winter westerly jet; the two cores of the westerly jet were well-simulated by this model. Song and Zhou (2013) suggested that the FGOALS-s2 model underestimated the jet intensity in summer. Previous studies have generally revealed that the multimodel ensemble mean (MME) of CMIP5 can not only predict the interannual variation in the EASWJ well (Dai and Lu, 2013; Ma et al., 2015; Ren et al., 2017), but can also reasonably simulate the relationship between summertime precipitation over Central and Eastern Asia and the jet stream (Zhao et al., 2018; Yan et al., 2019). However, systematic defects still exist in EASWJ simulations among different CMIP5 models, such as variations in the jet intensity and meridional position (Lin et al., 2019), and these discrepancies increase the CMIP5 simulation uncertainty and challenge the reliability of climate projections. The Coupled Model Intercomparison Project Phase 6 (CMIP6) models, then, were designed to address these new challenges and scientific issues (Eyring et al., 2016). Compared to the CMIP5 version, the CMIP6 GCMs were improved to be able to further describe past, present, and future climate conditions. Recent studies have indicated that the simulations of some variables by CMIP6 GCMs are better than those obtained with CMIP5 GCMs (Fernandez-Granja et al., 2021; Xiao et al., 2021). Jet stream simulations have been slightly improved in CMIP6 GCMs, and the magnitude of deviation is substantially lower than that of the past-stage CMIP models (Harvey et al., 2020); however, some CMIP6 models even perform worse than the CMIP5 models. Therefore, the abilities of CMIP6 models to simulate the jet stream must be evaluated urgently before these models can be applied to climate change-related research.

To comprehensively evaluate the EASWJ simulations performed by the climate models, we must obtain a set of indices to describe the characteristics of the EASWJ, as discussed in previous studies (Lin and Lu, 2005; Liu et al., 2010; Zhao et al., 2018). According to the definition given by Kuang and Zhang (2006), the jet axis index is defined as the mean latitude of the maximum westerlies in the upper troposphere across the longitudes spanning the East Asian continent; the jet axis index directly and objectively describes the meridional displacement of the jet. Most past studies defined the jet intensity index as the averaged zonal wind velocity in the target area (Yang and Zhang, 2007; Yang, 2015; Wang and Zuo, 2016). However, the location and range of the EASWJ are constantly changing, and calculating the location and intensity of the EASWJ by delineating a fixed range is not sufficiently accurate. To improve the accuracy of these jet indices, in this paper, we proposed a new self-adaptive algorithm to redefine the jet meridional displacement index and intensity index. In addition, we introduced a jet width index to characterize the width of the EASWJ and used these indices to evaluate the model performance.

Compared to qualitative assessments, quantitative assessments of climate models are more intuitive and accurate for scientific research (Stanfield et al., 2016) and are thus of great scientific significance for improving climate projections. Therefore, the purposes of this paper were to quantitatively evaluate the abilities of CMIP5 and CMIP6 models

to simulate the EASWJ using the three jet indices defined in this study and to provide a comprehensive assessment of the EASWJ. The rest of the paper is organized as follows. Section 2 describes the data used in this study. Section 3 introduces the new algorithms used to define the three jet indices. In Section 4, we quantitatively evaluate the EASWJ simulations performed by the CMIP5 and CMIP6 GCMs. Section 5 screens 12 groups of models, describes their simulation performances, and explores the possible reasons for simulation deviations among the CMIP5 and CMIP6 GCMs. The major conclusions and discussions are summarized in Section 6.

2. Datasets

The monthly 200-hPa zonal wind (U200) velocity and air temperature data were obtained from a reanalysis dataset of the European Center for Medium-Range Weather Forecasts (ECMWF) called the ECMWF reanalysis (ERA-Interim) product (Dee et al., 2011); this product has a horizontal resolution of $1.0^\circ \times 1.0^\circ$. The monthly precipitation data used in this study were obtained from the Global Precipitation Climatology Project (GPCP; Adler et al., 2003). To allow comparisons to the ERA-Interim reanalysis results, one more reanalysis dataset was obtained from the National Centers for Environment Prediction/Department of Energy Atmospheric Model Intercomparison Project II (NCEP2; Kanamitsu et al., 2002) and used in our study. Due to the almost identical performances of the NCEP2 reanalysis dataset and the ERA-Interim product, only the results of the ERA-Interim reanalysis dataset are discussed in the following research.

In addition, the monthly mean 200-hPa zonal wind velocity and air temperature values derived from the historical simulations of the 25 CMIP5 GCMs and 25 CMIP6 GCMs were compared with those in the ERA-Interim reanalysis dataset. The specific information of each model is provided in Table 1, including the name, country, and resolution of each model. The simulations were first regressed to a resolution of $1.0^\circ \times 1.0^\circ$ to ensure consistency with the reanalysis datasets. All simulations covered the 1979–2005 period.

3. Methods

3.1. U200 climatology

The EASWJ is a stable circulation system with evident seasonal variations. In winter, the EASWJ intensity reaches its peak, corresponding to a central intensity over 70 m/s and a southerly location (Fig. 1d). The intensity of the jet gradually weakens from winter to summer, and its position shifts northward (Fig. 1a, b, and d). The EASMJ moves to its northernmost position in summer, at which time the jet intensity reaches its weakest point throughout the year (Fig. 1b). Ye et al. (1958) had noticed that the general circulation of the Northern Hemisphere experienced sudden changes in June and October, and the significant feature associated with these fluctuations is the change in the westerlies. Fig. 2 shows the evolution of the meridional precipitation and U200 distributions averaged between 1979 and 2005. The jet axis is stable at approximately 30°N from January to April and then swiftly shifts northward from April to July. The jet axis reaches approximately 41°N in August, retreats southward from September to November, and gradually returns to approximately 30°N . This behavior reveals that the intensity and position of the EASWJ undergo evident seasonal changes. In addition, the jet width also changes significantly throughout the year, indicating that not only the intensity and location but also the coverage of the EASWJ are constantly changing. It is worth noting that there is a good consistency between the movement of the rain belt and the meridional displacement of the jet. The EASWJ is usually located on the northern edge of the rain belt, suggesting that the EASWJ can indicate the position of the rain belt over East Asia well. Based on the climatology of the EASWJ, three indices are required to describe the location, intensity, and width of the jet when assessing the simulation performances

Table 1

Basic information of the 25 CMIP5 GCMs and 25 CMIP6 GCMs analyzed in this paper.

CMIP5 GCMs			CMIP6 GCMs		
Model name	Country	Resolution	Model name	Country	Resolution
ACCESS1-0	Australia	192 × 145	ACCESS-CM2	Australia	192 × 145
ACCESS1-3	Australia	192 × 145	ACCESS-ESM1-5	Australia	192 × 144
BCC-CSM1-1	China	128 × 64	BCC-CSM2-MR	China	320 × 160
BCC-CSM1-1-m	China	128 × 64	BCC-ESM1	China	128 × 64
CanESM2	Canada	128 × 64	CanESM5	Canada	128 × 64
CESM1-BGC	America	288 × 192	CESM2	America	288 × 192
CMCC-CM	Italy	480 × 240	CESM2-FV2	America	144 × 96
CMCC-CMS	Italy	192 × 96	CESM2-WACC	America	288 × 192
FGOALS-g2	China	128 × 60	CMCC-CM2-HR4	Italy	288 × 192
FIO-ESM	China	128 × 64	CMCC-ESM2	Italy	288 × 192
GFDL-CM3	America	144 × 90	FGOALS-g3	China	180 × 80
GFDL-ESM2G	America	144 × 90	FIO-ESM-2.0	China	288 × 192
GFDL-ESM2M	America	144 × 90	GFDL-CM4	America	280 × 180
GISS-E2-H	America	144 × 90	GISS-ESM4	America	280 × 180
GISS-E2-H-CC	America	144 × 90	GISS-E2-1-G-CC	America	144 × 90
GISS-E2-R	America	144 × 90	GISS-E2-1-G	America	144 × 90
GISS-E2-R-CC	America	144 × 90	GISS-E2-1-H	America	144 × 90
IPSL-CM5A-LR	France	96 × 96	IPSL-CM5A2-INCA	France	96 × 96
IPSL-CM5A-MR	France	144 × 143	MIROC6	Japan	256 × 128
MIROC5	Japan	256 × 128	MPI-ESM-1-2-HAM	German	192 × 96
MPI-ESM-LR	German	192 × 96	MPI-ESM1-2-HR	German	384 × 192
MPI-ESM-MR	German	192 × 96	MPI-ESM1-2-LR	German	192 × 96
MRI-CGCM3	Japan	320 × 160	MRI-ESM2-0	Japan	320 × 160
NorESM1-M	Norway	144 × 96	NorESM2-LM	Norway	144 × 96
NorESM1-ME	Norway	144 × 96	NorESM2-MM	Norway	288 × 192

of the CMIP5 and CMIP6 GCMs.

3.2. New algorithms for subtropical westerly jet indices

According to the traditional definition of the subtropical westerly jet, in the middle and upper troposphere, wind belts with wind speeds greater than 30 m/s can be considered westerly jets (Sheng, 1986; Zou et al., 1990; Zhu et al., 2000). Most studies use this threshold ($U_{200} = 30$ m/s) to identify westerly jets (Zhang and Kuang, 2005, Zhang et al., 2008; Dong et al., 2011; Zhang and Zeng, 2020). Due to the weakness of summer jets, some studies have used 25 m/s or even 20 m/s to identify areas in which westerly jets are located (Kuang and Zhang, 2005; Shen et al., 2011). Based on these previous studies in combination with the actual situation of our study, we used a wind speed threshold of 30 m/s in spring, autumn, and winter and a wind speed threshold of 25 m/s in summer. To describe the EASWJ characteristics as accurately as possible, we limited the calculation scope to areas in which the zonal wind was greater than the 200-hPa threshold in the definitions of the intensity and meridional position index. In addition to the above two indices, which have commonly been used in previous studies, the jet

width index was also introduced to quantitatively characterize the EASWJ coverage. In the EASWJ index calculations performed in our study, we restricted the longitudinal range to East Asia; due to concerns about the occurrence of certain extremes and the location uncertainties in the model simulations, we restricted the latitude range to the Northern Hemisphere only. The jet boundary positions and algorithms of the three indices used in this paper are given below.

- (1) To determine the north and south jet boundary positions, across each longitude line, if $u_i \geq 30\text{m/s}$ and $u_{i-1} < 30\text{m/s}$, the averaged latitude of point i was set as the jet south boundary position; if $u_i \geq 30\text{m/s}$ and $u_{i+1} < 30\text{m/s}$, the averaged latitude of point i was set as the jet north boundary position (we used 25 m/s as the corresponding threshold in summer).
- (2) To calculate the jet meridional displacement index, in areas where the U_{200} value was greater than 30 m/s, we determined the averaged latitude of the points corresponding to the maximum U_{200} across each longitude line (25 m/s was used as the threshold in summer).
- (3) To calculate the jet intensity index, the average U_{200} value within the self-adaptive north and south boundaries was defined as the jet intensity index.
- (4) To calculate the jet width index, the latitudinal difference between the north and south boundary positions was determined.

To assess the jet index values calculated using the traditional algorithms (fixed area) and new algorithms (self-adaptive area), we compared the abilities of two jet meridional position indices to indicate precipitation anomalies in the middle and lower reaches of the YRV (28°N–33°N, 108°E–122°E; Fig. 3). The annual average coverage of the EASWJ (25°N–45°N, 70°E–140°E) was selected as the fixed area in the traditional algorithm. The index values calculated using the two methods illustrate the seasonal evolution patterns and interannual variations in the EASWJ (Fig. 3c). However, the meridional displacement index calculated by the self-adaptive algorithm was more significantly correlated with precipitation in the YRV (Fig. 3a), and the northward shift of the EASWJ reduced precipitation in the YRV; this was consistent with the findings of previous studies. Furthermore, we averaged precipitation over the YRV and obtained the interannual precipitation variation; from this, we observed that the jet index obtained using the new algorithm was significantly negatively correlated (-0.53) with precipitation in the YRV (Fig. 3c). Overall, the self-adaptive-area algorithm proposed in our study is more suitable for capturing the features of the EASWJ throughout the year than the traditional algorithm. Thus, the three new jet indices were used to assess the EASWJ simulations derived based on multiple CMIP5 and CMIP6 GCMs in this study.

4. Quantitative evaluations of the CMIP5 and CMIP6 GCMs

Before we quantitatively evaluated the EASWJ, the overall performances of the 25 CMIP5 and 25 CMIP6 models used in this paper were investigated. The spatial patterns of the U_{200} biases derived between the multimodel ensemble means (MMEs) of the CMIP5 and CMIP6 models and the pattern reflected in the reanalysis data were comparable. From spring to autumn, the deviations between the simulations and reanalysis data displayed a “+ – +” pattern from south to north in the Northern Hemisphere (Fig. 4a-c and 4e-g), indicating that the CMIP5 and CMIP6 MMEs overestimated the U_{200} in the low and high latitudes of East Asia while significantly underestimating the values in the mid-latitude jet region. As a result, the meridional shear of the modeled horizontal wind decreased and may have been caused to some extent by the related atmospheric dynamics processes simulated by the GCMs. U_{200} deviations in winter are very insignificant in the core area of the EASWJ, generally below 1 m/s, with significant positive deviations in the upstream area of the EASWJ (Fig. 4d and h). Throughout the year, the EASWJ intensity was seriously underestimated in summer by the

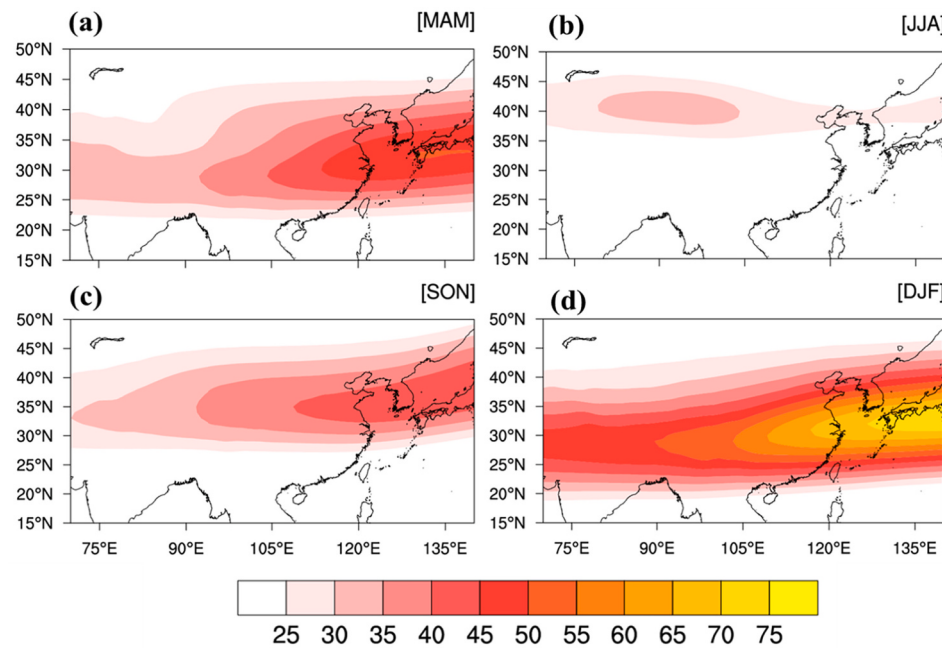


Fig. 1. Climatological mean U200 values ($m \cdot s^{-1}$) derived from the ERA-Interim dataset in spring (a), summer (b), autumn (c), and winter (d) during the 1979–2005 period.

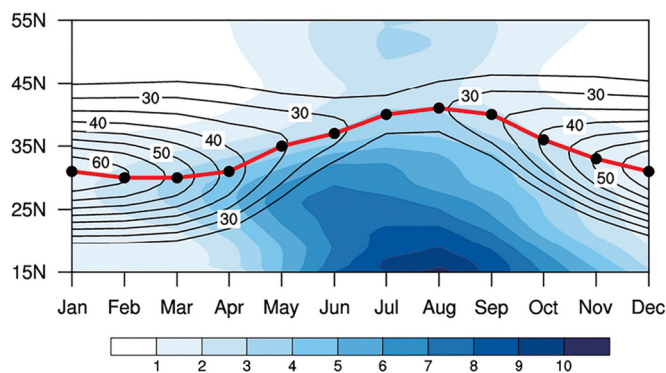


Fig. 2. Seasonal evolution behaviors of the meridional distributions (averaged between 90° E and 120° E) of the climatological mean U200 (contour; $m \cdot s^{-1}$) and precipitation (shaded; mm/day) derived from the ERA-Interim dataset and GPCP from 1979 to 2005. The thick red line represents the jet axis, and the solid black circle represents the jet core. (For interpretation of the references to colour in this figure legend, the reader is referred to the web version of this article.)

CMIP5 MME (Fig. 4b). However, the largest negative U200 deviations output by the CMIP6 MME occurred in spring (Fig. 4e). It is worth noting that the U200 differences between the CMIP6 MME and the reanalysis dataset were symmetrically distributed along the jet axis in summer (Fig. 4f), causing the simulated EASWJ to shift northward. Overall, the CMIP5 and CMIP6 MMEs could both capture the EASWJ features but produced regional differences and U200 magnitude errors.

To further assess the jet characteristic represented in the MMEs of the two-stage models, the jet indices were compared by season (Fig. 5). The CMIP5 MME displayed good skills when simulating the jet location and intensity (Fig. 5a-b), although the simulated jet intensity was weaker in summer, while the jet coverage was wider (Fig. 5c). The CMIP6 MME was comparable to the CMIP5 MME but expressed even larger deviations (Fig. 5d-f). In contrast, the CMIP models exhibited relatively small inter-model differences in winter, suggesting that the model simulations were more consistent in months in which the EASWJ is relatively strong

compared to weak-EASWJ months. Overall, regarding the EASWJ simulation results, the MME of the new-stage models reflected no significant enhancement over the models of the previous phase.

4.1. Representations of the EASWJ intensity

Despite the CMIP5 and CMIP6 MMEs being able to capture the EASWJ characteristics, apparent differences were observed between the models (Lin et al., 2019). Fig. 6 shows the jet intensity biases derived between the CMIP5 (CMIP6) GCM simulations and the reanalysis results. Among the 25 CMIP5 models, 13 underestimated the EASWJ intensity (Fig. 6a), while 11 simulated jets with stronger intensities than that indicated by the reanalysis data in most months. Some of the models exhibited relatively low jet intensity index deviations in all months, such as FIO-ESM, GFDL-CM3. Furthermore, the annual cumulative discrepancy in the FIO-ESM model was even less than that of the CMIP5 MME. However, the MIROC5 model had significant biases and grossly underestimated the EASWJ intensity in spring and summer. Through a detailed analysis, we found that most climate models from the same organization had comparable results. For instance, GISS-E2-R, GISS-E2-R-CC, GISS-E2-H, and GISS-E2-H-CC all simulate extremely strong EASWJs. However, the BCC-CSM1-1, BCC-CSM1-1-m, GFDL-CM3, and GFDL-ESM2G models showed distinctive performances. The CMIP5 GCMs reflected an apparent seasonal differences in the jet intensity simulation bias. The biases of most CMIP5 GCMs in spring and summer, especially in spring, were larger than those in other seasons.

Fig. 6b indicates that the EASWJ intensities simulated by the CMIP6 GCMs in most seasons were weaker than the reanalysis results; this was consistent with the above analysis (Fig. 4e-g). The annual cumulative deviations in the jet intensities simulated by the NorESM2-LM, FIO-ESM-2-0, GFDL-CM4, and GFDL-ESM4 models were similar to the MME results, while those of the GISS-E2-1-G-CC, GISS-E2-1-G, GISS-E2-1-H, and IPSL-CM5A-INCA models were above 12 m/s. The new versions of some of the best-performing CMIP5 models (e.g., FIO-ESM, GFDL-CM3, GFDL-ESM2G) still reflected the best performances in CMIP6. Moreover, some new model versions reflected significant jet intensity simulation improvements, such as the ACCESS-CM2, BCC-CSM2-MR, FGOALS-g3, MPI-ESM1-2-HR, NorESM2-LM, and NorESM2-MM models. However,

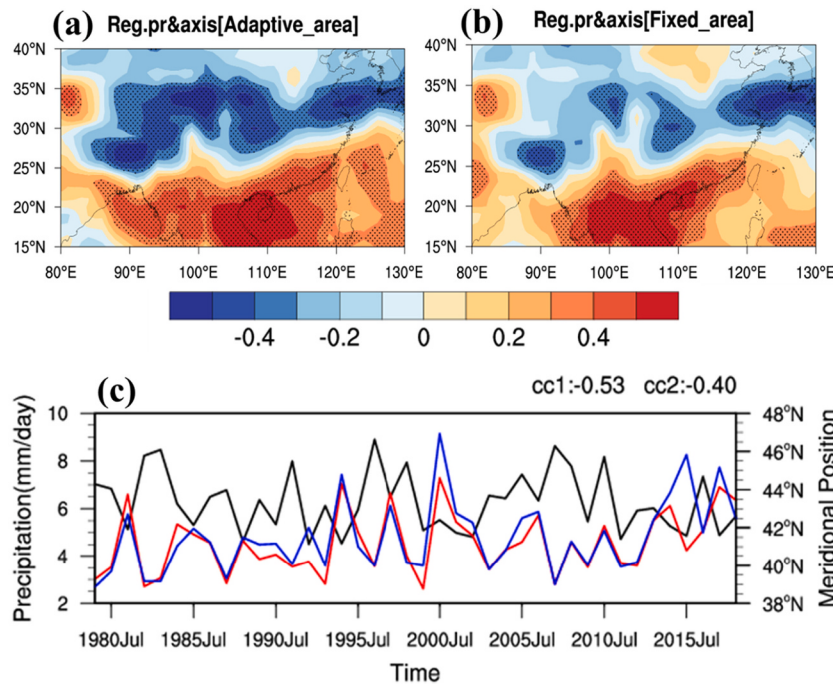


Fig. 3. Correlation coefficients of precipitation and the jet meridional displacement index values calculated using the self-adaptive-area algorithm (a) and the fixed-area algorithm (b) in July; (c) time series of YRV precipitation (black lines) and jet meridional displacement index values calculated using the fixed-area algorithm (red lines) and the self-adaptive-area algorithm (blue lines) in July from 1979 to 2018. The data presented were sourced from the ERA-Interim and GPCP reanalysis products. In the upper right corner of (c), cc1 indicates correlation coefficient of precipitation and the jet meridional displacement index values calculated using the self-adaptive-area algorithm; cc2 indicates correlation coefficient of precipitation and the jet meridional displacement index values calculated using the fixed-area algorithm. (For interpretation of the references to colour in this figure legend, the reader is referred to the web version of this article.)

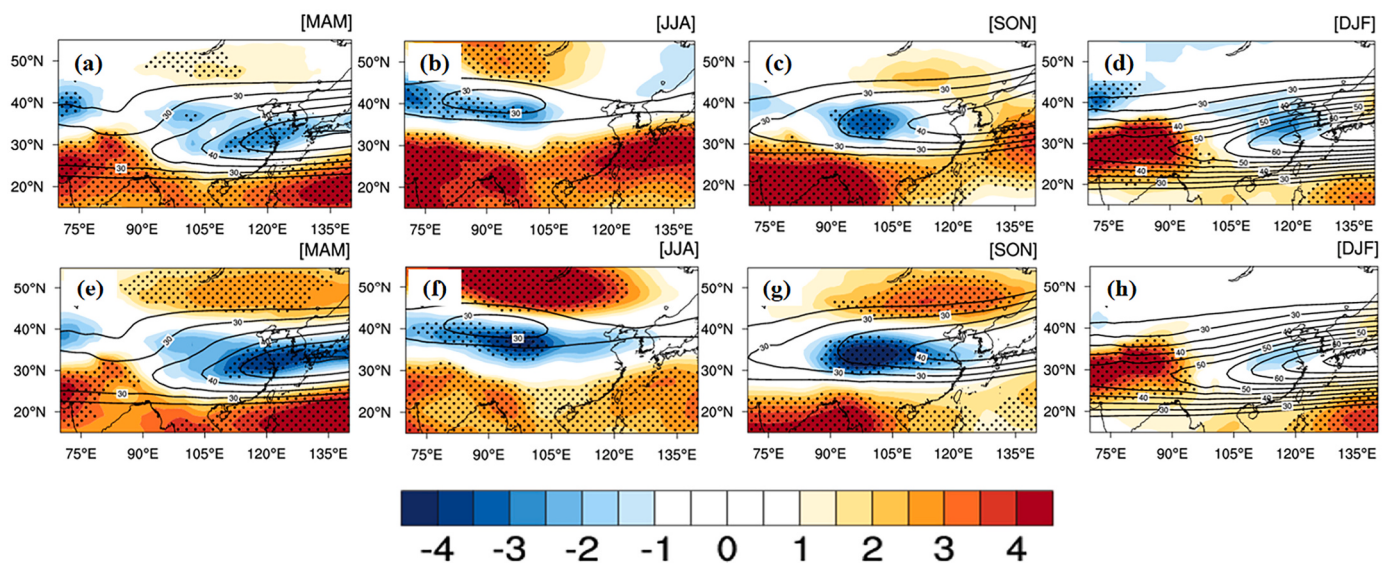


Fig. 4. U200 differences (shaded; $m \cdot s^{-1}$) derived between the CMIP5 (a-d) (CMIP6 (e-h)) MME simulation and the ERA-interim reanalysis data in the East Asian region and the climatological mean U200 values derived from the reanalysis data (contour; ms^{-1}) in spring (a, e), summer (b, f), autumn (c, g), and winter (d, h) averaged over the 1979–2005 period. The dots indicate that a majority of models agree with this result, exceeding the 95% confidence level.

some new model versions performed worse than their counterparts in CMIP5; GISS-E2-1-G-CC, GISS-E2-1-G, and GISS-E2-1-H in CMIP6 not only showed worse skills but also exhibited distinctive results.

4.2. Representations of EASWJ meridional displacement

Next, the assessment of the meridional jet displacement index was investigated (Fig. 7). Among the 25 CMIP5 models, 9 simulated northward-shifting jets; the maximum annual cumulative deviation was above 8° in the MPI-ESM-LR. In contrast, 9 models simulated southward-shifting jets, with MRI-CGCM3 deriving the maximum annual cumulative deviation of 7° . The deviations in the CMCC-CM, GFDL-ESM2G, and GFDL-ESM2M model results were even below 1° per season.

Nevertheless, the jet meridional position simulations output by some models from the same organization were consistent (e.g., MPI-ESM-LR and MPI-ESM-MR; IPSL-CM5B-LR and IPSL-CM5A-MR; and GISS-E2-R, GISS-E2-R-CC, GISS-E2-H, and GISS-E2-H-CC). Likewise, seasonal differences were observed in the meridional jet displacement simulation biases; for example, the simulation performances were significantly worse in summer and autumn, especially in autumn, than the other seasons. These results suggest that in weak-EASWJ seasons, the location of the jet was not captured accurately.

Regarding the meridional jet position simulations of the CMIP6 GCMs (Fig. 7b), most models exhibited consistent results and tended to simulate northward EASWJs; this behavior was opposite that of CMIP5. The performances of ACCESS-CM2, CMCC-CM2-HR4, GFDL-CM4,

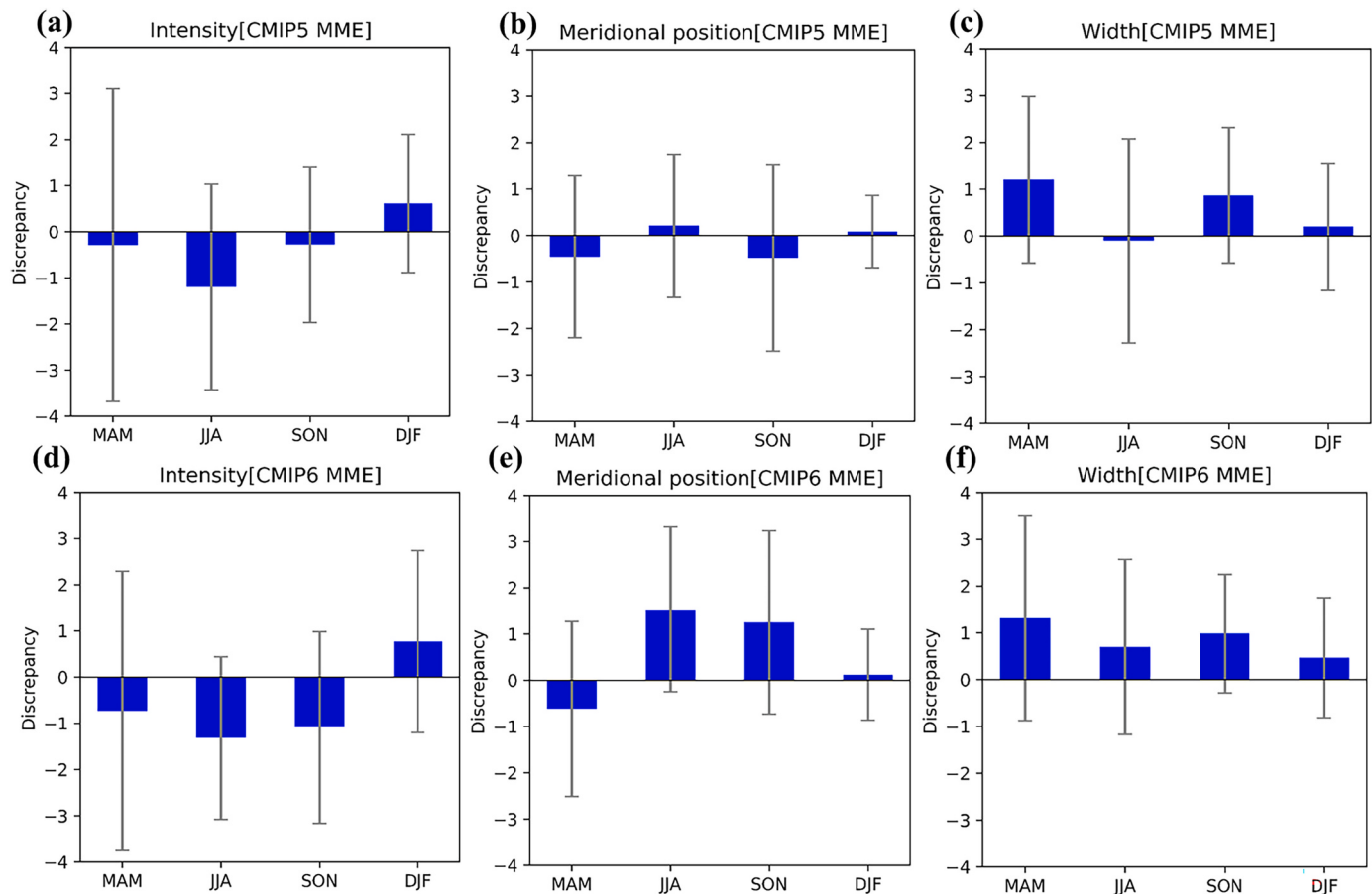


Fig. 5. EASWJ characteristic differences between the CMIP5 (CMIP6) MME simulation and the reanalysis results in the four seasons. Panels (a), (b), and (c) show the differences in intensity, meridional position, and width simulated by the CMIP5 MME, while panel (d), (e), and (f) are the same as (a), (b) and (c), but for the CMIP6 MME. The gray error bars indicate the inter-model spread.

GFDL-ESM4, and MIROC6 even exceeded that of the CMIP6 MME. Likewise, a consistent seasonal differences in the jet location deviations was reflected by the CMIP6 GCM simulations. For example, in summer and autumn, the CMIP6 GCMs showed reduced abilities to reproduce the meridional position of the EASWJ, and the simulated EASWJs were thus located significantly northward. In contrast to the CMIP5 models (Fig. 7a), the overall biases were increased in CMIP6 models, although ACCESS-CM2, BCC-ESM1, CanESM5, MIROC6, MRI-ESM2-0, and MPI-ESM1-2-HR performed better than their CMIP5 predecessors.

4.3. Representations of the EASWJ width

Compared to the representations of the first two indices, the jet width index simulation results obtained using the CMIP5 and CMIP6 GCMs showed consistent broadening (Fig. 8), and the MME results were the same (Fig. 5c and f). The annual cumulative jet width deviations simulated by 13 of the CMIP5 models were substantially small. Among these models, MPI-ESM-LR and GISS-E2-H-CC showed good performances, approaching that of the CMIP5 MME (Fig. 8a). The CMCC-CM, CMCC-CMS, IPSL-CM5A-MR, and IPSL-CM5B-LR models produced larger deviations than the other models. Similar to the jet intensity and position indices, the simulated jet width biases also reflected seasonal differences.

After assessing the jet widths simulated by the CMIP6 GCMs, the results suggest that the inter-model jet width simulation diversity among the CMIP6 GCMs was lower than those of the other two indices (Fig. 8b). Furthermore, the annual cumulative deviations produced by the GFDL-CM4 and GFDL-ESM4 models were substantially lower than that of the

MME results. Compared to the CMIP5 models, the results of the CMIP6 models showed a significant tendency to overestimate the EASWJ coverage. No apparent seasonal differences were found in the jet width simulation biases derived for the CMIP6 models.

Overall, most CMIP5 GCMs showed remarkable abilities to represent the EASWJ, but the performance of the models varies greatly. The CMIP5 models did not have consistent properties in terms of their EASWJ intensity and location simulations, while most CMIP5 GCMs tended to simulate relatively wide-coverage jets. Most CMIP6 models reflected consistent EASWJ simulation tendencies and tended to simulate significantly weak, northerly, and wide jets. A few CMIP6 models reflected improved abilities to simulate the EASWJ intensity and location compared to their predecessors in CMIP5.

5. Possible causes of simulation deviations in the CMIP5 and CMIP6 GCMs

We evaluated the results obtained for the three jet indices to divide the analyzed models into two groups according to their performances. We chose the three best-performing models and the three worst-performing models with regard to each index to perform further analyses, as shown in Table 2 and Table 3. The twelve selected model groups among the CMIP5 and CMIP6 models were as follows: Intensity_Top3 (FIO-ESM, GFDL-CM3, and GFDL-ESM2G), Intensity_Last3 (IPSL-CM5A-LR, MIROC5, and IPSL-CM5A-MR), Axis_Top3 (GFDL-ESM2M, GFDL-ESM2G, and CMCC-CM), Axis_Last3 (MPI-ESM-LR, FGOALS-g2, and BCC-CSM1-1), Width_Top3 (MPI-ESM-LR, GISS-E2-H-CC, and GISS-E2-H), and Width_Last3 (CMCC-CMS, IPSL-CM5A-MR, and CMCC-CM) for

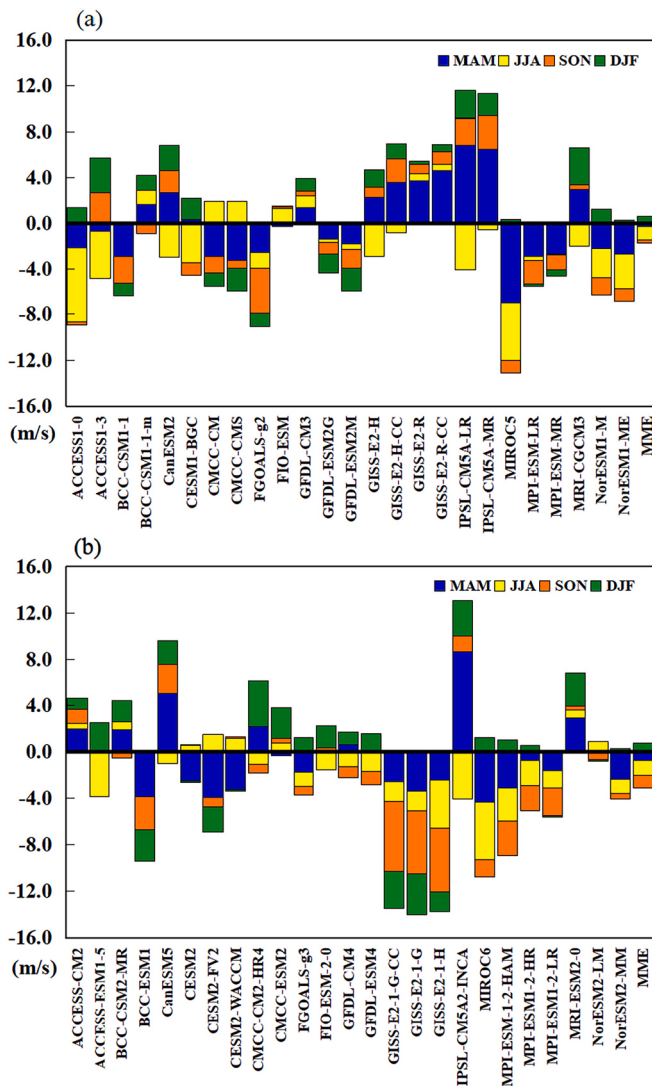


Fig. 6. Jet intensity differences between the simulations of the 25 CMIP5 GCMs (a) and the reanalysis results. Panel (b) is the same as panel (a) but reflects the 25 CMIP6 GCM results. The MME simulations are also shown in the chart. The colored bars denote each season, as shown in the legend, and the black line represents the “0 deviation line.” The bar below the black line denotes that the jet intensity results obtained in the corresponding month are underestimated and vice versa. The height of each bar shows the magnitude of the deviation.

the CMIP5 models and Intensity_Top3 (NorESM2-LM, CESM2, and FIO-ESM-2-0), Intensity_Last3 (IPSL-CM5A2-INCA, GISS-E2-1-G, and GISS-E2-1-H), Axis_Top3 (ACCESS-CM2, MIROC6, and GFDL-ESM4), Axis_Last3 (GISS-E2-1-G, FGOALS-g3, and GISS-E2-1-H), Width_Top3 (GFDL-CM4, GFDL-ESM4, and NorESM2-MM), and Width_Last3 (ACCESS-CM2, CanESM5, and GISS-E2-1-G-CC) for the CMIP6 models.

To verify that the selected model groups could effectively capture the EASWJ characteristics, we compared the simulated U200 meridional distribution with the reanalysis results. By calculating the zonal average (90°E - 120°E) and meridional distribution of U200, the meridional jet position, intensity, and width can be derived. As expected, the U200 meridional distributions simulated by the Intensity_Top3, Axis_Top3, and Width_Top3 groups coincided with the reanalysis data in winter, while in spring and summer, the deviations were slightly larger (Fig. 9). This finding was consistent with the above analysis. We also selected the worst-performing models listed in Table 2 and Table 3 as a control experiment. The U200 meridional distributions simulated by the Intensity_Last3, Axis_Last3, and Width_Last3 for the CMIP5 deviated

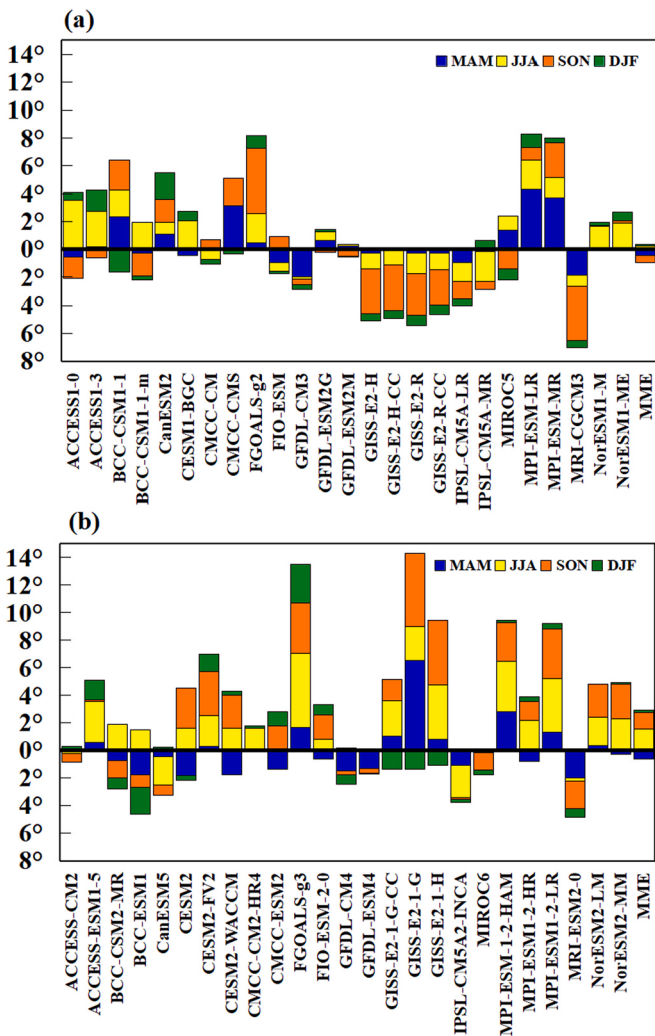


Fig. 7. Same as Fig. 6 but for the jet meridional displacement index values simulated by the 25 CMIP5 GCMs (a) and 25 CMIP6 GCMs (b). A bar below the black line denotes that the simulated jet was shifted southward compared to the reanalysis data result and vice versa.

significantly in both spring and summer. Fig. 10 shows that the U200 distribution simulated by the Intensity_Top3, Axis_Top3, and Width_Top3 groups of CMIP6 models coincided with the reanalysis data throughout the year. The U200 meridional distributions in the Intensity_Last3 and Axis_Last3 models differed critically from the reanalysis results. Overall, the three jet indices presented in this study can be used to evaluate the simulation ability of a model, and the model groups selected in our quantitative evaluation could effectively capture the characteristics of the EASWJ.

Furthermore, we investigated the possible causes associated with the worst-performing models that could not accurately reproduce the characteristics of the EASWJ. Based on the thermal wind principle, the altitudinal variation in the zonal wind is proportional to the meridional temperature gradient (Zhang et al., 2006; Huang et al., 2015). Therefore, the meridional temperature gradient can be used to explore the possible causes of simulation deviations among the poorly performing models. In this study, we defined the meridional temperature difference (MTD) as the air temperature at the north position minus that at the south position at a 1.0° latitudinal interval. According to this definition, negative MTDs usually occur at 200 hPa in the mid-latitudes of the Northern Hemisphere. Among the many CMIP models, we randomly selected the best and worst models from Table 2 and Table 3 and obtained comparative springtime and summertime results using the worst

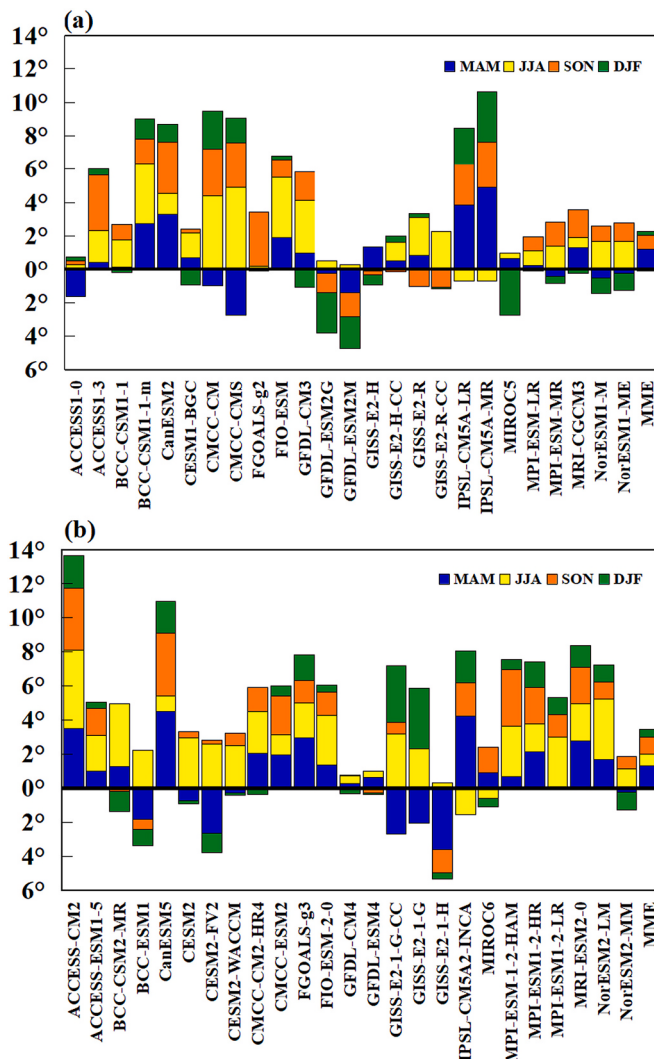


Fig. 8. Same as Fig. 6 but for the jet width index simulations obtained with the 25 CMIP5 GCMs (a) and 25 CMIP6 GCMs (b). A bar below the black line denotes that the simulated jet width was thinner than that reflected in the reanalysis data and vice versa.

Table 2
Best- and worst-performing CMIP5 models.

intensity (better)	intensity (worse)	Position (better)	Position (worse)	Width (better)	Width (worse)
FIO-ESM	IPSL- CM5A-LR	GFDL- ESM2M	MPI-ESM- LR	MPI- ESM-LR	CMCC- CM
GFDL-CM3	MIROC5	GFDL- ESM2G	FGOALS- g2	GISS-E2- H-CC	IPSL- CM5A-MR
GFDL-ESM2G	IPSL- CM5A-MR	CMCC-CM	BCC- CSM1-1	MPI- ESM-LR	CMS

simulations as examples. Fig. 11 shows the mean U200 and MTD (vertically averaged from 500 hPa to 200 hPa) states in the results of the randomly selected models and reanalysis product. The results indicate that a well-matching relationship exists between the U200 and MTD fields in the reanalysis data, and the location of the jet region approaches the large-MTD-value area. The model results also reflect a corresponding relationship between the wind field and the MTD field. For instance, the well-performing models could better reproduce the mid-latitude MTD distributions and could simulate more accurate jet characteristics.

Table 3
Best- and worst-performing CMIP6 models.

intensity (better)	intensity (worse)	Position (better)	Position (worse)	Width (better)	Width (worse)
NorESM2- LM	IPSL- CM5A2- INCA	ACCESS- CM2	GISS- E2-1-G	GFDL-CM4	ACCESS- CM2
CESM2	GISS- E2-1-G	MIROC6	FGOALS- g3	GFDL- ESM4	GFDL- ESM4
FIO-ESM- 2-0	GISS- E2-1-H	GFDL- ESM4	GFDL- ESM4	NorESM2- MM	GISS- E2-1-G- CC

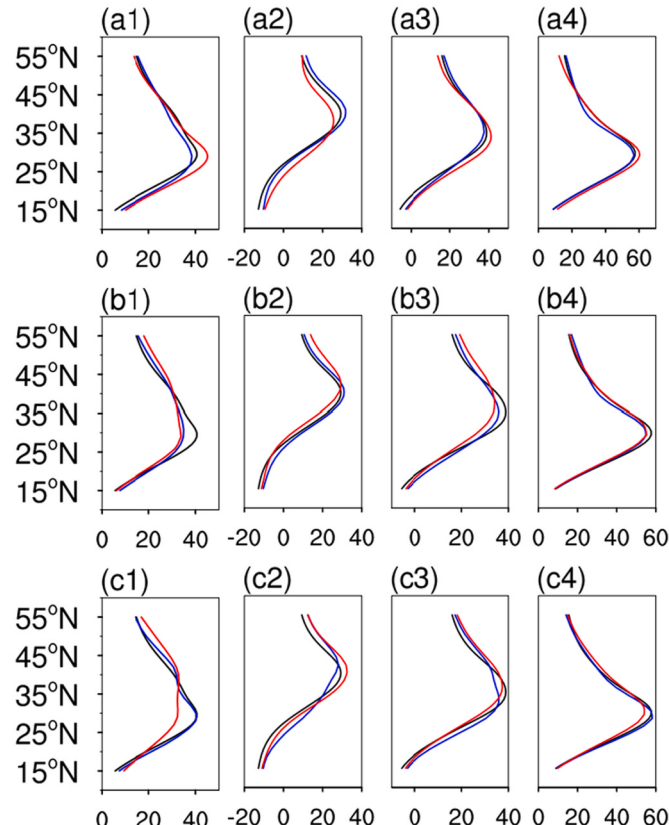


Fig. 9. Comparison of the meridional distributions (averaged between 90°E and 120°E; $m \cdot s^{-1}$) of U200 between the reanalysis results (black lines) and the Intensity_Top3 (blue lines), Intensity_Last3 (red lines; panels a1-a4), Axis_Top3 (blue lines), Axis_Last3 (red lines; panels b1-b4), Width_Top3 (blue lines), or Width_Last3 (red lines; panels c1-c4) CMIP5 models in spring (a1, b1, and c1), summer (a2, b2, and c2), autumn (a3, b3, and c3), and winter (a4, b4, and c4) averaged over the 1979–2005 period. (For interpretation of the references to colour in this figure legend, the reader is referred to the web version of this article.)

Nevertheless, the MTD pattern represented by the poorly performing models was very different from the reanalysis results. To some extent, the quality of EASWJ simulation results depends on the climatic pattern of the temperature field.

To further explore the influence of the temperature field on jet characteristics in climate models, we calculated the regression fields of the MTD and three indices in the reanalysis data and model outputs (Figs. 12 and 13). The models shown in Figs. 12 and 13 were selected according to the quantitative evaluation of the simulations of the three jet indices by the CMIP5 and CMIP6 GCMs (Figs. 6–8) and corresponded to the models with minimum or maximum deviation. Columns 1–3 in Figs. 12 and 13 show the regression fields of MTD and jet intensity,

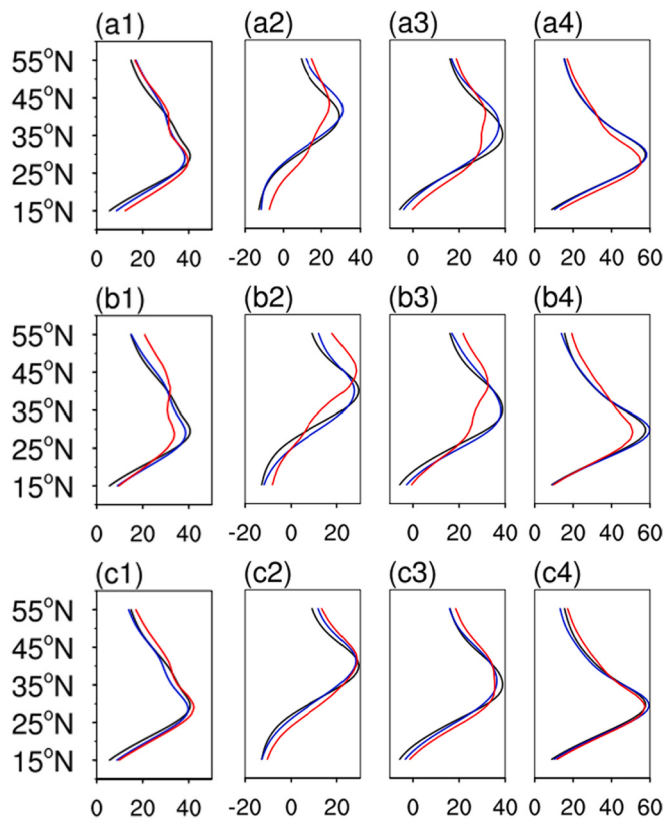


Fig. 10. Comparison of the monthly U_{200} meridional distribution (averaged between 90°E and 120°E ; $m \cdot s^{-1}$) between the reanalysis results (black lines) and Intensity_Top3 (blue lines), Intensity_Last3 (red lines; panels a1-a4), Axis_Top3 (blue lines), Axis_Last3 (red lines; panels b1-b4), Width_Top3 (blue lines), or Width_Last3 (red lines; panels c1-c4) results of CMIP6 models in spring (a1, b1, and c1), summer (a2, b2, and c2), autumn (a3, b3, and c3), and winter (a4, b4, and c4) averaged over the 1979–2005 period. (For interpretation of the references to colour in this figure legend, the reader is referred to the web version of this article.)

position, and width index. To standardize the results, we selected the season corresponding to the largest simulation deviations.

In the reanalysis results, the MTD anomaly associated with a change in the jet intensity was located in the coverage area of the westerlies (Fig. 12a), while that related to the meridional EASWJ position was roughly distributed on the north and south sides of the jet axis (Fig. 12b). The MTD anomalies that affected the change in the jet range were mainly distributed in the EASWJ coverage region (Fig. 12c). The best-performing CMIP5 GCMs could capture the interannual variation relationships between MTD and the jet characteristics; in addition, the magnitudes and distributions of the MTD anomalies were similar among these models. For example, the FIO-ESM, GFDL-ESM2M, and MPI-ESM-LR models reproduced the EASWJ characteristics well, but the simulated EASWJ intensity was weaker, so the associated MTD anomaly was also weaker than that reflected in the reanalysis data (Fig. 12d-f). The MTD anomaly patterns derived from the three worst-performing models, shown in the last row of Fig. 12, were very different from those in the reanalysis data (Fig. 12g-i). Overall, the representations of the EASWJ by the CMIP5 GCMs had a certain degree of dependence on the MTD simulation results. In the CMIP6 models, similar results appeared (Fig. 13). Therefore, the MTD may be one possible cause, but not the decisive factor, in the representation of the EASWJ by CMIP6 GCMs.

The above analysis concludes that the models selected by the quantitative evaluation method proposed in this paper are reliable. The well-performing models could represent the MTD distribution and interannual variation more accurately than the remaining models. The

simulations of the climatic state of the MTD and its correlation with interannual changes in the EASWJ affect the EASWJ simulation performance. Therefore, the meridional temperature gradient is a relevant factor. However, complex dynamics and thermal processes are involved in the analyzed models, and the other factors affecting the simulations of jet characteristics by climate models need to be further explored.

6. Summary

As a crucial component of the atmospheric circulation system, the EASWJ critically impacts the weather and climate in East Asia. Based on the significance of the EASWJ, we conducted an assessment of the state-of-the-art GCMs from CMIP5 and CMIP6, with a focus on EASWJ simulations. We proposed a new self-adaptive algorithm for detecting the jet boundaries and defined the intensity index, meridional displacement index, and width index of the EASWJ to comprehensively describe the characteristics of the EASWJ in terms of its intensity, location, and coverage.

The evaluation results suggest that the CMIP5 and CMIP6 MMEs roughly exhibited relatively minor deviations in their representation of EASWJ characteristics; however, noteworthy differences were observed among models. Through a quantitative analysis of the differences between the CMIP5 model outputs and the reanalysis product, we found that the jet intensities simulated by some CMIP5 models, such as FIO-ESM and GFDL-CM3, were similar to the reanalysis results. The deviations in the jet meridional displacement index simulated by CMCC-CM, GFDL-ESM2G, and GFDL-ESM2M were substantially lower than those simulated by other models. More than half of the CMIP5 models displayed a prominent ability to simulate the EASWJ width. Overall, the CMIP5 GCMs generally tended to simulate wider jets, but no consistent tendency was found in the jet intensity or location simulation results. Moreover, most CMIP5 GCMs performed relatively poorly in spring and summer, and a considerable inter-model spread was detected among the CMIP5 models.

Unlike the CMIP5 GCMs, the EASWJ simulations performed by the CMIP6 GCMs exhibited a more evident and consistent tendency, and most CMIP6 models tended to simulate significantly weaker, wider, and more-northward jets than the CMIP5 models. The jet intensities simulated by half of the CMIP6 models were similar to that reflected in the reanalysis data. The annual cumulative meridional jet displacement deviations simulated by the ACCESS-CM2, CMCC-CM2-HR4, and MIROC6 models were even lower than that of the CMIP6 MME. The GFDL-CM4 and GFDL-ESM4 models could accurately simulate the EASWJ range. However, most CMIP6 models could not accurately reproduce the EASWJ characteristics in summer or autumn. Compared to the CMIP5 models, although significant improvements in the representation of the jet intensity were observed in some CMIP6 models, some of the models attained similar or even worse results than their CMIP5 counterparts with regards to the location and coverage of the EASWJ.

Further analysis revealed that the CMIP5 and CMIP6 model groups selected using the quantitative evaluation method presented in this study could more accurately simulate the U_{200} meridional distribution. Then, the possible reasons for this result were detected using the thermal wind principle. The MTD simulation performance was found to be a salient factor in the EASWJ simulations, including both the mean MTD pattern and its interannual correlation with the EASWJ characteristics. However, the mechanisms and processes that drive the EASWJ are complex, and previous studies have shown that the formation of the EASWJ is related to momentum, eddy transport, topography, and thermal differences between land and sea (Ye and Zhu, 1958; Lee and Kim, 2003; Kuang et al., 2007; Li and Wettstein, 2012; Zhang et al., 2019; Chan et al., 2020). Interactions between atmospheric disturbance waves and the EASWJ have also been reported in previous studies (Gao, 1952; Gao et al., 1989; Gao and Shiyan, 1991). Atmospheric disturbance waves can transport heat and momentum to the latitudinal mean airflow region, thus accelerating the EASWJ. In addition, the designs of the

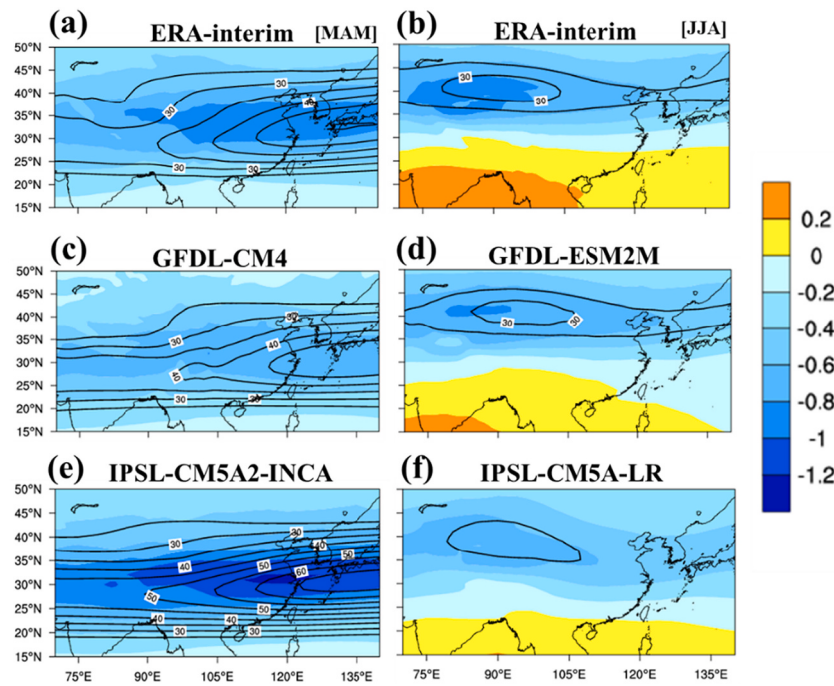


Fig. 11. Climatological mean 200-hPa zonal wind (contour; $m \cdot s^{-1}$) and 200–500-hPa averaged meridional temperature difference (shaded; K) in summer (a, c, e) and spring (b, d, f) during the 1979–2005 period.

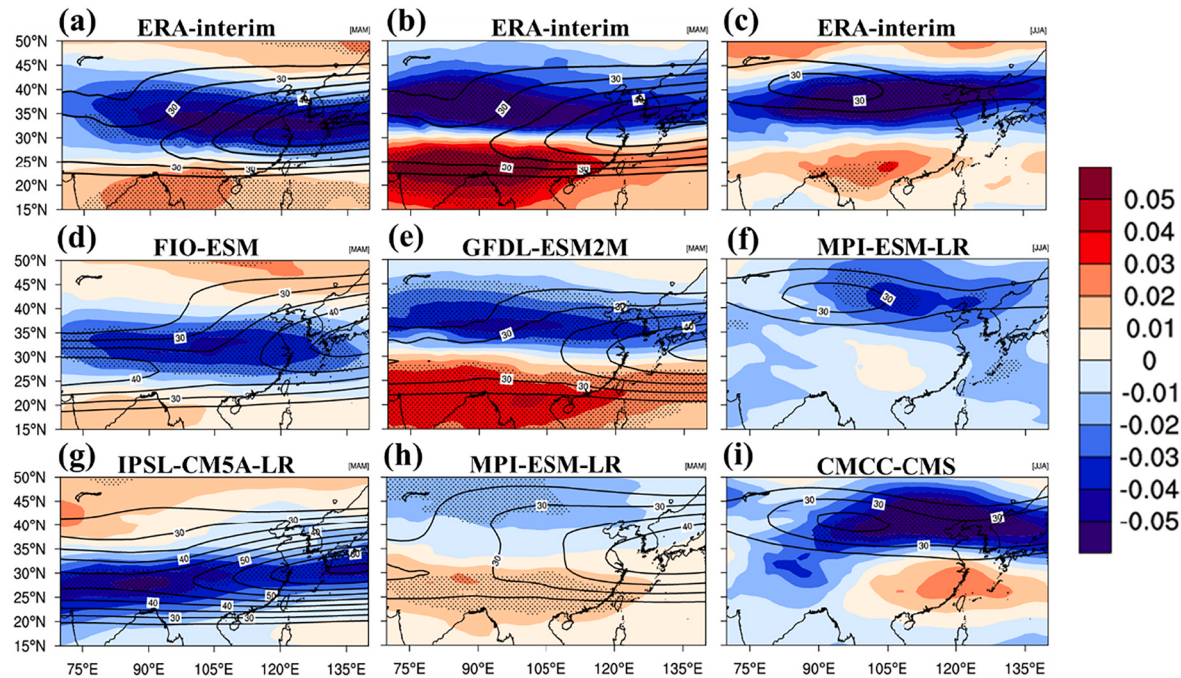


Fig. 12. The 200–500-hPa averaged meridional temperature difference (shaded; K) regressed onto the jet intensity index (a, d, and g), meridional displacement index (b, e, and h), and width index (c, f, and i) of the reanalysis data and the selected CMIP5 model outputs. The dots indicate that the relationship exceeds the 95% confidence level, as determined using a two-tailed *t*-test. The isolines represent the climatological mean 200-hPa zonal wind (contour; $m \cdot s^{-1}$).

analyzed models are very sophisticated, and different model designs can lead to different simulation results. Other causes of the observed simulation biases need to be investigated in future work. Notably, not all new-stage GCMs in CMIP6 reflect improvements, and the reasons for these decreasing capabilities of some new models deserve further exploration.

From the results of the quantitative evaluation, we found that both the CMIP5 models and CMIP6 models simulated the summertime

EASWJ poorly compared to the other three seasons. However, a large number of previous studies have shown that summertime EASWJ anomalies can cause precipitation changes or even floods and droughts; thus, in the future, additional prognostic studies will focus on the changes in the summertime EASWJ. Given the results of our evaluation, we believe that when models are used in studies related to the summertime EASWJ, researchers should be careful when selecting appropriate models based on the summertime EASWJ model simulation

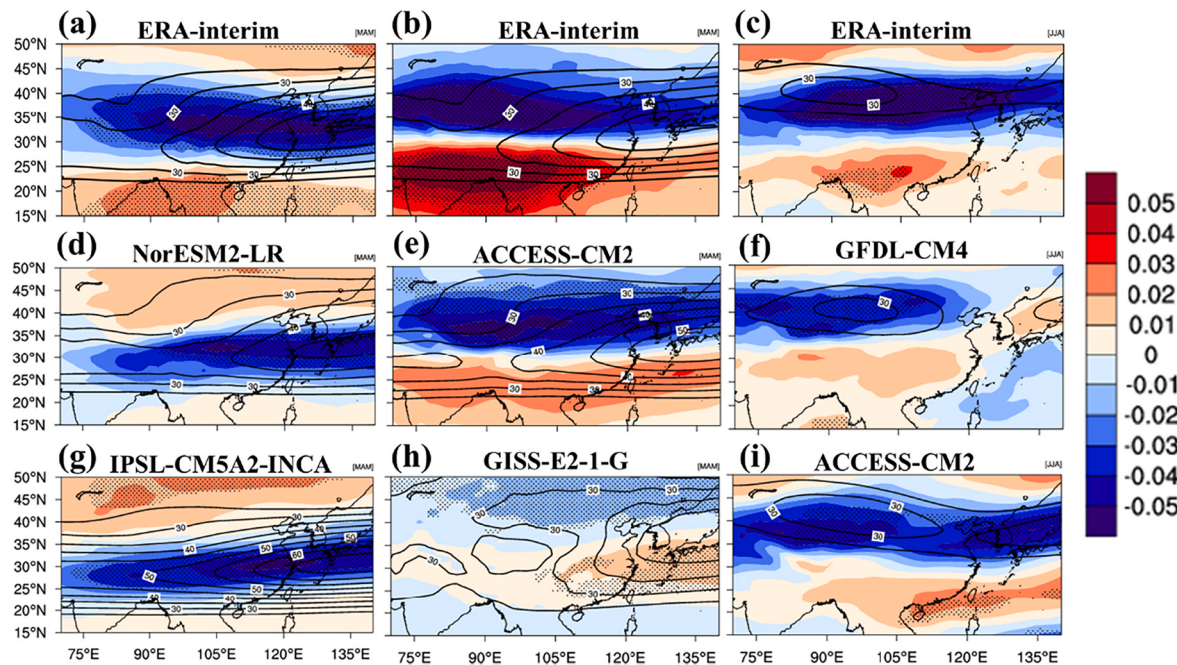


Fig. 13. The 200–500-hPa averaged meridional temperature difference (shaded; K) regressed onto the jet intensity index (a, d, and g), meridional displacement index (b, e, and h), and width index (c, f, and i) of the reanalysis data and the selected CMIP6 model outputs. The dots indicate that the relationship exceeds the 95% confidence level, as determined using a two-tailed t-test. The isolines represent the climatological mean 200-hPa zonal wind (contour; $m \cdot s^{-1}$).

results. Specifically, the quantitative evaluation method presented in this paper provides a relatively reliable basis for selecting CMIP5 and CMIP6 GCMs. Moreover, this study also provides an improved method of using CMIP models in future predictions. When using these models to predict future climate conditions, first, a simple model evaluation can be conducted to filter out the models that are most suitable for the study; then, the ensemble mean of these best-performing models can be applied to help researchers obtain future climate trends with increased reliability. In particular, the significant differences among models remind us that we should be careful when using GCMs to explain EASWJ responses.

CRediT authorship contribution statement

Bingqian Zhou: Conceptualization, Software, Investigation, Formal analysis, Writing – original draft, Writing – review & editing, Visualization. **Shujuan Hu:** Conceptualization, Software, Resources, Investigation, Writing – review & editing, Project administration, Funding acquisition. **Yongli He:** Conceptualization, Software, Writing – review & editing. **Siyi Wang:** Writing – original draft, Writing – review & editing. **Deqian Li:** Writing – original draft, Writing – review & editing. **Guolin Feng:** Project administration, Funding acquisition.

Declaration of Competing Interest

The authors declare that they have no known competing financial interests or personal relationships that could have appeared to influence the work reported in this paper.

Acknowledgments

This work was funded by the National Key Research and Development Program of China (Grant Nos.2019YFA0607104) and the National Natural Science Foundation of China (Grant Nos. 41975076, 41775069). We have no any potential sources of conflict of interest. The authors thank the European Center for Medium-Range Weather Forecasts (ECMWF) for providing the ERA-Interim reanalysis (<https://www.ecmwf.int/en/forecasts/datasets/browse-reanalysis-datasets>), National Centers for Environment Prediction/Department of Energy Atmospheric Model Intercomparison Project II (NCEP2) for supplying the reanalysis data (<https://psl.noaa.gov/data/gridded/data.ncep.reanalysis2>), Global Precipitation Climatology Project (GPCP) for offering precipitation data (<https://climatedataguide.ucar.edu/climate-data/gpcp-daily-global-precipitation-climatology-project>), the World Climate Research Programme (WCRP) for providing CMIP5 experiments datasets (<https://esgf-node.llnl.gov/search/cmip5/>) and CMIP6 experiments datasets (<https://esgf-node.llnl.gov/search/cmip6/>).

(ecmwf.int/en/forecasts/datasets/browse-reanalysis-datasets), National Centers for Environment Prediction/Department of Energy Atmospheric Model Intercomparison Project II (NCEP2) for supplying the reanalysis data (<https://psl.noaa.gov/data/gridded/data.ncep.reanalysis2>), Global Precipitation Climatology Project (GPCP) for offering precipitation data (<https://climatedataguide.ucar.edu/climate-data/gpcp-daily-global-precipitation-climatology-project>), the World Climate Research Programme (WCRP) for providing CMIP5 experiments datasets (<https://esgf-node.llnl.gov/search/cmip5/>) and CMIP6 experiments datasets (<https://esgf-node.llnl.gov/search/cmip6/>).

References

- Adler, R.F., et al., 2003. The version-2 global precipitation climatology project (GPCP) monthly precipitation analysis (1979–present). *J Hydrometeorol* 4, 1147–1167. [https://doi.org/10.1175/1525-7541\(2003\)004<1147:TGCP>2.0.CO;2](https://doi.org/10.1175/1525-7541(2003)004<1147:TGCP>2.0.CO;2).
- Bao, Y., You, Q., 2019. How do westerly jet streams regulate the winter snow depth over the Tibetan Plateau? *Clim Dyn* 53 (1–2), 353–370. <https://doi.org/10.1007/s00382-018-5489-1>.
- Bracegirdle, T.J., Hyder, P., Holmes, C.R., 2018. CMIP5 diversity in Southern Westerly jet projections related to historical sea ice area: strong link to strengthening and weak link to shift. *J Clim* 31 (1), 195–211. <https://doi.org/10.1175/JCLI-D-17-0320.1>.
- Chan, D., Zhang, Y., Wu, Q., et al., 2020. Quantifying the dynamics of the interannual variabilities of the wintertime East Asian Jet Core. *Clim Dyn* 54, 2447–2463. <https://doi.org/10.1007/s00382-020-05127-3>.
- Chiang, J.C.H., Kong, W., Wu, C.H., Battisti, D.S., 2020. Origins of East Asian Summer monsoon seasonality. *J Clim* 33 (18), 7945–7965. <https://doi.org/10.1175/JCLI-D-19-0888.1>.
- Dai, Y., Liu, R.Y., 2013. Projected change in the relationship between East Asian summer rainfall and upper-tropospheric westerly jet. *Chin Sci Bull* 58 (12), 1436–1442. <https://doi.org/10.1007/s11434-012-5540-1>.
- Dee, D.P., Uppala, S.M., Simmons, A.J., Berrisford, P., Poli, P., Kobayashi, S., Andrae, U., Balmaseda, M.A., Balsamo, G., Bauer, P., Bechtold, P., Beljaars, A.C.M., van de Berg, L., Bidlot, J., Bormann, N., Delsol, C., Dragan, R., Fuentes, M., Geer, A.J., Vitart, F., 2011. The ERA-Interim reanalysis: configuration and performance of the data assimilation system. *Q J R Meteorol Soc* 137 (656), 553–597. <https://doi.org/10.1002/qj.828>.
- Dong, L., Guo, P., Wang, P., Qi, L., 2011. Impact of the variation of westerly jets over East Asia on precipitation of eastern China in July. *Sci Cold Arid Reg* 3 (5), 408–418. <https://doi.org/10.3724/SP.J.1226.2011.00408>.
- Du, Y., Zhang, Y., Xie, Z., 2008. Impacts of longitude location changes of east Asian westerly jet core on precipitation distribution during meiyu period in middle-lower reaches of Yangtze River Valley(in Chinese). *Acta Meteorol Sin* 66 (4), 566–576. <https://doi.org/10.11676/qxb2008.054>.

- Du, Y., Zhang, Y., Xie, Z., 2009. Location variation of the East Asia subtropical Westerly Jet and its effect on the summer precipitation anomaly over Eastern China. Chinese J Geophys (in Chinese) 33 (3), 581–592. <https://doi.org/10.3878/j.issn.1006-9895.2009.03.15>.
- Du, Y., Li, T., Xie, Z., Zhu, Z., 2016. Interannual variability of the Asian subtropical westerly jet in boreal summer and associated with circulation and SST anomalies. Clim Dyn 46 (7–8), 2673–2688. <https://doi.org/10.1007/s00382-015-2723-x>.
- Eyring, V., Bony, S., Meehl, G.A., Senior, C.A., Stevens, B., Stouffer, R.J., Taylor, K.E., 2016. Overview of the coupled model intercomparison project phase 6 (CMIP6) experimental design and organization. Geosci Model Dev 9 (5), 1937–1958. <https://doi.org/10.5194/gmd-9-1937-2016>.
- Fang, X., Zeng, X., Chen, X., 2009. Spatial and temporal distribution characteristics of westerly jet in 200 hPa in east Asian and the analysis of relationship between it and summer precipitation in China(in Chinese). Meteorol Environ Sci 32 (2), 11–15. <https://doi.org/10.3969/j.issn.1673-7148.2009.02.003>.
- Feng, J., Wei, T., Dong, W., Wu, Q., Wang, Y., 2014. CMIP5/AMIP GCM simulations of East Asian summer monsoon. Adv Atmos Sci 31 (4), 836–850. <https://doi.org/10.1007/s00376-013-3131-y>.
- Fernandez-Granja, J.A., Casanueva, A., Bedia, J., et al., 2021. Improved atmospheric circulation over Europe by the new generation of CMIP6 earth system models. Clim Dyn 56, 3527–3540. <https://doi.org/10.1007/s00382-021-06562-9>.
- Gao, Y., 1952. Study on the winter westerly circulation over China based on the tropospheric air temperature. Acta Meteor Sinica Z1 (1–2), 50–62 (in Chinese).
- Gao, S., Shiyian, Tao, 1991. The lower layer frontogenesis induced by the acceleration of the upper jet stream. Chin J Atmos Sci 15 (2), 11–22. <https://doi.org/10.3878/j.issn.1006-9895.1991.02.02> (in Chinese).
- Gao, S., Tao, S., Ding, Y., 1989. The generalized E-P flux of wave-mean flow interactions. Sci China (Ser B) 32 (7), 774–784. CNKI:SUN:JBXK.0.1989-07-015, (in Chinese).
- Harvey, B.J., Cook, P., Shaffrey, L.C., Schiemann, R., 2020. The response of the northern hemisphere storm tracks and jet streams to climate change in the CMIP3, CMIP5, and CMIP6 climate models. J Geophys Res-Atmos 125. <https://doi.org/10.1029/2020JD032701>.
- He, S., Xu, X., Furevik, T., Gao, Y., 2020. Eurasian cooling linked to the vertical distribution of Arctic warming. Geophys Res Lett 47 (10) e2020GL087212.
- Huang, D.Q., Zhu, J., Zhang, Y.C., Huang, A.N., 2013. Uncertainties on the simulated summer precipitation over Eastern China from the CMIP5 models. J Geophys Res Atmos 118 (16), 9035–9047. <https://doi.org/10.1002/jgrd.50695>.
- Huang, D.Q., Zhu, J., Zhang, Y.C., Wang, J., Kuang, X.Y., 2015. The impact of the East Asian subtropical jet and polar front jet on the frequency of spring persistent rainfall over southern China in 1997–2011. J Clim 28 (15), 6054–6066. <https://doi.org/10.1175/JCLI-D-14-0064.1>.
- Huang, D.Q., Yan, P., Zhu, J., Zhang, Y., Kuang, X., Cheng, J., 2018. Uncertainty of global summer precipitation in the CMIP5 models: a comparison between high-resolution and low-resolution models. Theor Appl Climatol 132 (1–2), 55–69. <https://doi.org/10.1007/s00704-017-2078-9>.
- Kanamitsu, M., Ebisuzaki, W., Woollen, J., Yang, S.K., Hnilo, J.J., Fiorino, M., Potter, G. L., 2002. NCEP–DOE AMIP-II reanalysis (R-2). Bull Am Meteorol Soc 83 (11), 1631–1643. [https://doi.org/10.1175/bams-83-11-1631\(2002\)083<1631:nar>2.3.co;2](https://doi.org/10.1175/bams-83-11-1631(2002)083<1631:nar>2.3.co;2).
- Kuang, X.Y., Zhang, Y., 2005. Seasonal variation of the East Asian Subtropical Westerly Jet and its association with the heating field over East Asia. Adv Atmos Sci 22 (6), 831–840. <https://doi.org/10.1007/BF02918683>.
- Kuang, X.Y., Zhang, Y., 2006. Impact of the position abnormalities of East Asian subtropical westerly jet on summer precipitation in middle-lower reaches of Yangtze River. Plateau Meteorol 25 (3), 382–389. [https://doi.org/10.1016/S1003-6326\(06\)60040-X](https://doi.org/10.1016/S1003-6326(06)60040-X).
- Kuang, X., Zhang, Y., Liu, J., 2007. Seasonal variations of the East Asian Subtropical Westerly Jet and the thermal mechanism[J]. J Meteor Res 21 (2), 192–203. <https://doi.org/10.1029/2006JD007471>.
- Lau, K.M., Kim, K.M., Yang, S., 2000. Dynamical and boundary forcing characteristics of regional components of the Asian summer monsoon. J Clim 13 (14), 2461–2482. [https://doi.org/10.1175/1520-0442\(2000\)013<2461:DABFC>2.0.CO;2](https://doi.org/10.1175/1520-0442(2000)013<2461:DABFC>2.0.CO;2).
- Lee, S., Kim, H.-K., 2003. The dynamical relationship between subtropical and eddy-driven jets. J Atmos Sci 60 (12), 1490–1503.
- Li, X., Lu, R., 2017. Extratropical factors affecting the variability in summer precipitation over the Yangtze River Basin, China. J Clim 30 (20), 8357–8374. <https://doi.org/10.1175/JCLI-D-16-0282.1>.
- Li, X., Lu, R., 2018. Subseasonal change in the seesaw pattern of precipitation between the Yangtze River basin and the Tropical Western North Pacific during summer. Adv Atmos Sci 35 (10), 1231–1242. <https://doi.org/10.1007/s00376-018-7304-6>.
- Li, C., Wettstein, J.J., 2012. Thermally driven and eddy-driven jet variability in reanalysis*. J Clim 25 (5), 1587–1596. <https://doi.org/10.1175/JCLI-D-11-00145.1>.
- Li, C., Wang, J.-T., Lin, S.-Z., Cho, H.-R., 2004. The relationship between East Asian summer monsoon activity and northward jump of the upper Westerly Jet location(in Chinese). Chin J Atmos Sci 28 (5), 641–658. CNKI:SUN:DQXK.0.2004-05-000.
- Li, H., He, S., Gao, Y., Chen, H., Wang, H., 2020. North Atlantic modulation of interdecadal variations in hot drought events over northeastern China. J Clim 33 (10), 4315–4332. <https://doi.org/10.1175/JCLI-D-19-0440.1>.
- Liang, C., Frauenfeld, O.W., 2014. A comprehensive evaluation of precipitation simulations over China based on CMIP5 multimodel ensemble projections. J Geophys Res-Atmos 119 (10), 5767–5786. <https://doi.org/10.1002/2013JD021190>.
- Liang, X., Wang, W.-C., 1998. Associations between China monsoon rainfall and tropospheric jets. Q J R Meteorol Soc 124 (552), 2597–2623. <https://doi.org/10.1002/qj.49712455204>.
- Liao, Z., Zhang, Y., 2013. Concurrent variation between the East Asian subtropical jet and polar front jet during persistent snowstorm period in 2008 winter over southern China. J Geophys Res-Atmos 118 (12), 6360–6373. <https://doi.org/10.1002/jgrd.50558>.
- Liao, Q., Gao, S., Wang, H., Tao, S., 2004. Anomalies of the extratropical westerly jet in the north hemisphere and their impacts on east Asian summer monsoon(in Chinese). Chin J Geophys 47 (1), 10–18. <https://doi.org/10.3321/j.issn:0001-5733.2004.01.003>.
- Lin, Z., Lu, R., 2005. Interannual meridional displacement of the East Asian upper-tropospheric jet stream in summer. Adv Atmos Sci 22 (2), 199–211. <https://doi.org/10.1007/BF02918509>.
- Lin, Z., Fu, Y., Lu, R., 2019. Intermodel diversity in the zonal location of the climatological East Asian Westerly Jet core in summer and association with rainfall over East Asia in CMIP5 models. Adv Atmos Sci 36 (6), 614–622. <https://doi.org/10.1007/s00376-019-8221-z>.
- Liu, F., He, J., Jiang, A., 2010. Relationship between Asia Summer Westerly Wind Index and Summer Rainfall in China(in Chinese). J Nanjing Inst Meteorol 29 (4), 517–525. <https://doi.org/10.3969/j.issn.1674-7097.2006.04.012>.
- Lu, R., 2004. Associations among the components of the East Asian summer monsoon system in the meridional direction. J Meteorol Soc Jpn 82 (1), 155–165. <https://doi.org/10.2151/jmsj.82.155>.
- Lu, R.-Y., Oh, J.-H., Kim, B.-J., 2002. A teleconnection pattern in upper-level meridional wind over the North African and Eurasian continent in summer. Tellus A 54 (1), 44–55. <https://doi.org/10.3402/tellusa.v54i1.12122>.
- Ma, J., Xu, H., Lin, P., 2015. Meridional position biases of East Asian subtropical jet stream in CMIP5 models and their relationship with ocean model resolutions. Int J Climatol 35 (13), 3942–3958. <https://doi.org/10.1002/joc.4256>.
- Qiang, X.M., Yang, X.Q., 2008. Onset and end of the first rainy season in South China. Chinese J Geophys (in Chinese) 51 (5), 1333–1345. <https://doi.org/10.3321/j.issn:0001-5733.2008.05.007>.
- Ren, Y., Zhou, B., Song, L., Xiao, Y., 2017. Interannual variability of western North Pacific subtropical high, East Asian jet and East Asian summer precipitation: CMIP5 simulation and projection. Quat Int 440, 64–70. <https://doi.org/10.1016/j.quaint.2016.08.033>.
- Sampe, T., Xie, S.P., 2010. Large-scale dynamics of the meiyu-baiu rainband: environmental forcing by the westerly jet. J Clim 23 (1), 113–134. <https://doi.org/10.1175/2009JCLI3128.1>.
- Schiemann, R., Lüthi, D., Schär, C., 2009. Seasonality and interannual variability of the westerly jet in the Tibetan Plateau region. J Clim 22 (11), 2940–2957. <https://doi.org/10.1175/2008JCLI2625.1>.
- Shen, B.Z., Da Lin, Z., Lu, R.Y., Lian, Y., 2011. Circulation anomalies associated with interannual variation of early- and late-summer precipitation in Northeast China. Sci China Earth Sci 54 (7), 1095–1104. <https://doi.org/10.1007/s11430-011-4173-6>.
- Sheng, C., 1986. Pandect of Climate in China. Science Press, Beijing, pp. 85–89 (in Chinese).
- Song, F., Zhou, T., 2013. FGOALS-s2 simulation of upper-level jet streams over East Asia: mean state bias and synoptic-scale transient eddy activity. Adv Atmos Sci 30 (3), 739–753. <https://doi.org/10.1007/s00376-012-2212-7>.
- Stanfield, R.E., Jiang, J.H., Dong, X., Xi, B., Su, H., Donner, L., Rotstayn, L., Wu, T., Cole, J., Shindo, E., 2016. A quantitative assessment of precipitation associated with the ITCZ in the CMIP5 GCM simulations. Clim Dyn 47 (5–6), 1863–1880. <https://doi.org/10.1007/s00382-015-2937-y>.
- Tao, S., Zhao, Y., Chen, X., 1958. The relationship between May-Yu in far east and the behavior of circulation over Asia(in Chinese). Acta Meteorol Sin 29 (2), 119–134. <https://doi.org/10.11676/qxb1958.014>.
- Taylor, K.E., Stouffer, R.J., Meehl, G.A., 2012. An overview of CMIP5 and the experiment design. Bull Am Meteorol Soc 93 (4), 485–498. <https://doi.org/10.1175/BAMS-D-11-00094.1>.
- Wang, S., Zuo, H., 2016. Effect of the East Asian westerly jet's intensity on summer rainfall in the Yangtze River valley and its mechanism. J Clim 29 (7), 2395–2406. <https://doi.org/10.1175/JCLI-D-15-0259.1>.
- Wang, Z., Xu, Y., Zhou, B., 2017a. Evaluation of the CMIP5 models in simulating the change of the East Asian winter monsoon indices and their relationship with the wintertime atmospheric circulation and temperature(in Chinese). Chin J Geophys 60 (9), 3315–3324. <https://doi.org/10.6038/cjg20170904>.
- Wang, S., Zuo, H., Zhao, S., Zhang, J., Lu, S., 2017b. How East Asian westerly jet's meridional position affects the summer rainfall in Yangtze-Huaihe River Valley? Clim Dyn 51 (11–12), 4109–4121. <https://doi.org/10.1007/s00382-017-3591-3>.
- Wang, S., Zuo, H., Yin, Y., Wang, J., Ma, X., 2019. Asymmetric impact of East Asian jet's variation on midsummer rainfall in North China and Yangtze River Valley. Clim Dyn 53 (9–10), 6199–6213. <https://doi.org/10.1007/s00382-019-04923-w>.
- Wang, S., Hou, Y., Zhou, S., Zuo, H., Sun, F., Luo, J., 2021. Effect of circulation variation associated with East Asian jet on spring rainfall over North China and Yangtze-Huaihe River Valley. Atmos Res 258. <https://doi.org/10.1016/j.atmosres.2021.105611>.
- Wei, W., Zhang, R., Wen, M., Yang, S., 2017. Relationship between the Asian westerly jet stream and summer rainfall over Central Asia and North China: roles of the Indian Monsoon and the South Asian high. J Clim 30 (2), 537–552. <https://doi.org/10.1175/JCLI-D-15-0814.1>.
- Xiao, L., Yla, B., Mwa, B., Yj, A., Xda, B., 2021. Assessment of the coupled model intercomparison project phase 6 (cmip6) model performance in simulating the spatial-temporal variation of aerosol optical depth over eastern Central China. Atmos Res 261. <https://doi.org/10.1016/j.atmosres.2021.105747>.
- Xiao, C., Zhang, Y., 2013. Simulation of the westerly jet axis in boreal winter by the climate system model FGOALS-g2. Adv Atmos Sci 30 (3), 754–765. <https://doi.org/10.1007/s00376-012-2167-8>.

- Xiao, C., Zhang, Y., Lofgren, B.M., Nie, Y., 2016. The concurrent variability of East Asian subtropical and polar-front jets and its implication for the winter climate anomaly in China. *J Geophys Res-Atmos* 175 (121), 6787–6801. <https://doi.org/10.1038/175238c0>.
- Xie, Z., Du, Y., Yang, S., 2015. Zonal extension and retraction of the subtropical westerly jet stream and evolution of precipitation over East Asia and the Western Pacific. *J Clim* 28 (17), 6783–6798. <https://doi.org/10.1175/JCLI-D-14-00649.1>.
- Xuan, S., Zhang, Q., Sun, S., 2011. Anomalous midsummer rainfall in Yangtze River-Huaihe River valleys and its association with the East Asia westerly jet. *Adv Atmos Sci* 28 (2), 387–397. <https://doi.org/10.1007/s00376-010-0111-3>.
- Yan, Y., Li, C., Lu, R., 2019. Meridional displacement of the East Asian upper-tropospheric westerly jet and its relationship with the East Asian summer rainfall in CMIP5 simulations. *Adv Atmos Sci* 36 (11), 1203–1216. <https://doi.org/10.1007/s00376-019-9066-1>.
- Yang, H., 2015. Comparison of the intensity and meridional position of the East Asian Jet Stream in Winter(in Chinese). *Q Sci* 35 (6), 1545–1548. <https://doi.org/10.11928/j.issn.1001-7410.2015.06.23>.
- Yang, L., Zhang, Q., 2007. Anomalous perturbation kinetic energy of Rossby wave along east Asian westerly jet association with summer rainfall in China (in Chinese). *Chin J Atmos Sci* 31 (4), 586–595.
- Yang, S., Lau, K.M., Kim, K.M., 2002. Variations of the East Asian jet stream and Asian-Pacific-American winter climate anomalies. *J Clim* 15 (1), 306–325. [https://doi.org/10.1175/1520-0442\(2002\)015<0306:voteaj>2.0.co;2](https://doi.org/10.1175/1520-0442(2002)015<0306:voteaj>2.0.co;2).
- Ye, D., Zhu, B., 1958. Some Basic Issues of the Atmospheric General Circulation(in Chinese). Science Press, Beijing, 159 pp.
- Ye, D., Tao, S., Li, M., 1958. The abrupt chance of circulation over northern hemisphere during June and October(in Chinese). *Acta Meteorol Sin* 29 (4), 249–263.
- Zhang, Y., Zeng, H., 2020. Recent progresses in the studies of the East Asian jet streams. *J Meteorol Sci (in Chinese)* 40 (5), 617–627. <https://doi.org/10.3969/2020jms.0070>.
- Zhang, Y., Kuang, X., 2005. Simulation of East Asian subtropical westerly jet deviation and seasonal variation of rain belt in eastern China. *Chin Sci Bull* 50 (13), 1395–1399. <https://doi.org/10.3321/j.issn:0023-074X.2005.13.017>.
- Zhang, Y., Kuang, X., Guo, W., Zhou, T., 2006. Seasonal evolution of the upper-tropospheric westerly jet core over East Asia (in Chinese). *Geophys Res Lett* 33 (11), 3–6. <https://doi.org/10.1029/2006GL026377>.
- Zhang, Y., Takahashi, M., Guo, L., 2008. Analysis of the east asian subtropical westerly jet simulated by cCSR/nies/frcg coupled climate system model. *J Meteorol Soc Jpn Ser II* 86 (2), 257–278. <https://doi.org/10.2151/jmsj.86.257>.
- Zhang, Y., Yan, P., Liao, Z., Huang, D., Zhang, Y., 2019. The Winter concurrent meridional shift of the East Asian Jet streams and the associated thermal conditions. *J Clim* 32 (7), 2075–2088. <https://doi.org/10.1175/JCLI-D-18-0085.1>.
- Zhao, Y., Yu, X., Yao, J., Dong, X., 2018. Evaluation of the subtropical westerly jet and its effects on the projected summer rainfall over Central Asia using multi-CMIP5 models. *Int J Climatol* 38 (February), e1176–e1189. <https://doi.org/10.1002/joc.5443>.
- Zhou, W., Xie, S.-P., Yang, D., 2019. Enhanced equatorial warming causes deep-tropical contraction and subtropical monsoon shift. *Nat Clim Chang* 9 (11), 834–839. <https://doi.org/10.1038/s41558-019-0603-9>.
- Zhu, Q., Lin, J., Shou, S., Tang, D., 2000. *Principles and Methods of Synoptic Meteorology*. Meteorological Press (in Chinese).
- Zou, J., Jiang, J., Wang, M., 1990. *Aeroclimatology*. Meteorological Press, Beijing, pp. 200–212 (in Chinese).